



HAL
open science

Ultra-low and ultra-broad-band nonlinear acoustic metamaterials

Xin Fang, Jihong Wen, Bernard Bonello, Jianfei Yin, Dianlong Yu

► **To cite this version:**

Xin Fang, Jihong Wen, Bernard Bonello, Jianfei Yin, Dianlong Yu. Ultra-low and ultra-broad-band nonlinear acoustic metamaterials. *Nature Communications*, 2017, 8 (1), pp.1288. 10.1038/s41467-017-00671-9 . hal-01636912

HAL Id: hal-01636912

<https://hal.sorbonne-universite.fr/hal-01636912v1>

Submitted on 17 Nov 2017

HAL is a multi-disciplinary open access archive for the deposit and dissemination of scientific research documents, whether they are published or not. The documents may come from teaching and research institutions in France or abroad, or from public or private research centers.

L'archive ouverte pluridisciplinaire **HAL**, est destinée au dépôt et à la diffusion de documents scientifiques de niveau recherche, publiés ou non, émanant des établissements d'enseignement et de recherche français ou étrangers, des laboratoires publics ou privés.



Distributed under a Creative Commons Attribution 4.0 International License

ARTICLE

DOI: 10.1038/s41467-017-00671-9

OPEN

Ultra-low and ultra-broad-band nonlinear acoustic metamaterials

Xin Fang¹, Jihong Wen¹, Bernard Bonello², Jianfei Yin¹ & Dianlong Yu¹

Linear acoustic metamaterials (LAMs) are widely used to manipulate sound; however, it is challenging to obtain bandgaps with a generalized width (ratio of the bandgap width to its start frequency) >1 through linear mechanisms. Here we adopt both theoretical and experimental approaches to describe the nonlinear chaotic mechanism in both one-dimensional (1D) and two-dimensional (2D) nonlinear acoustic metamaterials. This mechanism enables NAMs to reduce wave transmissions by as much as 20–40 dB in an ultra-low and ultra-broad band that consists of bandgaps and chaotic bands. With subwavelength cells, the generalized width reaches 21 in a 1D NAMs and it goes up to 39 in a 2D NAM, which overcomes the bandwidth limit for wave suppression in current LAMs. This work enables further progress in elucidating the dynamics of NAMs and opens new avenues in double-ultra acoustic manipulation.

¹Laboratory of Science and Technology on Integrated Logistics Support, National University of Defense Technology, Changsha, Hunan 410073, China.

²Institut des NanoSciences de Paris (INSP-UMR CNRS 7588), Université Pierre et Marie Curie, (Box 840) 4, Place Jussieu, 75252 Paris Cedex 05, France. Correspondence and requests for materials should be addressed to J.W. (email: wenjihong@vip.sina.com) or to B.B. (email: bernard.bonello@insp.jussieu.fr)

Acoustic metamaterials^{1–5} (AMs) are promising for many applications, including acoustic and vibration insulation^{6–8}, sound absorption⁹, cloaking^{10–12}, sensors⁴ and topological insulators¹³. Relatively broad low-frequency bands are desirable and most studies^{1–18} in this field have focused on linear AMs (LAMs) based on the sub-wavelength locally resonant (LR) mechanism^{1, 18}. However, LR bandgaps are generally narrow^{2, 3}. The generalized width of a band is $\gamma = (f_{\text{cut}} - f_{\text{st}})/f_{\text{st}}$, where f_{st} (f_{cut}) denotes the start (cutoff) frequency of the band. In theory⁵ $\gamma = \sqrt{1 + m_r/m_b} - 1$ for the LR band-gap, where m_r (m_b) is the mass of the resonator (the base media) in a meta-cell, for example, $\gamma \approx 0.22$ for $m_r = m_b/2$. Recent works couple the LR and Bragg bandgaps^{19, 20} to obtain a width $\gamma = 0.71$ in a one-dimensional (1D) LAM²¹ with a lattice constant $a \approx 2\lambda/5$ and $\gamma = 0.85$ in a two-dimensional (2D) LAM²² with $a \approx \lambda/4$, where λ refers to the wavelength at f_{st} . Therefore, obtaining a generalized width $\gamma > 1$ in LAMs remains a challenge. May nonlinearity help overcome this difficulty?

Similar to nonlinear electromagnetic metamaterials^{23–26} where desired nonlinear responses have been demonstrated^{27–31}, nonlinear acoustic metamaterials (NAMs) deserve special attention. When acoustic waves propagate within a nonlinear acoustic medium, such as Fermi–Pasta–Ulam chains^{32–34} or granular crystals^{35–38}, nonlinear phenomena including discrete breathers³⁹, solitons^{40, 41} and bifurcations⁴² can be observed. Acoustic diodes^{36, 43, 44}, rectification⁴⁵ and lenses⁴⁶ based on nonlinear media have been designed. However, the involved mechanisms hardly allow for simultaneous low-frequency and broadband properties; therefore, the discovery of new mechanisms is required for further progress.

For finite LAMs, bandgaps are stop bands; however, the broad passbands actually consist of dense resonances that localize energy to enhance incident waves. Recently, a mechanism was theoretically predicted in discrete NAMs^{47–49}: the chaotic bands. Chaos is an aperiodic long-term behavior in a deterministic/nonlinear system exhibiting a strong dependence on the initial conditions⁵⁰. In NAMs⁴⁹, chaotic bands are those passbands in which an incident low-frequency periodic wave becomes a chaotic emerging wave, reducing wave transmission. The chaotic wave features a high-frequency continuous spectrum evidencing the dispersion of energy^{47, 49}. These waves have lower amplitudes than the corresponding linear resonances; thus, NAMs can suppress wave propagation in the passbands. The wave suppression effect of the strong chaos is broadband and it depends on the frequency but not the width of the nonlinear LR bandgap⁴⁹. Therefore, we can design a NAM with nonlinear meta-cells that generate ultra-low frequency but narrow linearized LR bandgaps. When strong nonlinearities occur, the passbands higher than these nonlinear LR bandgaps become chaotic and wave propagation is suppressed; an ultra-low and ultra-broad (double-ultra) band NAM is thus obtained.

In this work, we report on NAMs based on the chaotic band that achieves double-ultra band wave suppression. We design both a 1D NAM beam and a 2D NAM plate with periodic strongly nonlinear sub-wavelength meta-cells. When the strong nonlinearity appears, our experiments demonstrate that the NAMs substantially suppress wave propagation in the double-ultra bands. By combining frequency responses, bifurcations, Lyapunov exponents and different experiments, we describe the propagation of waves and demonstrate that the double-ultra effect is induced by the chaotic waves.

Results

NAM design. As elucidated by the sketched band structure of the diatomic model (Fig. 1a, b), we propose 1D and 2D NAMs with

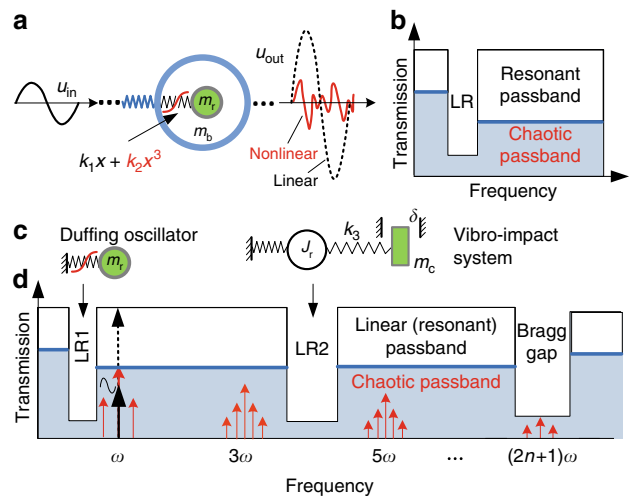


Fig. 1 Schematic and conceptual diagram. **a** Diatomic NAM model composed of periodic linear base m_b coupled with Duffing oscillators m_r through the nonlinear spring $k_1x + k_2x^3$, where k_1 and k_2 are the linear and nonlinear stiffness coefficients, respectively. **b** Its band structure. Here, the passbands become chaotic bands, where a periodic input wave u_{in} generates chaotic output wave (u_{out} red) with an amplitude is much lower than that of the corresponding linear resonance (u_{out} dashed black). **c** Two nonlinear sources in our NAM cell: Duffing oscillator and coupled vibro-impact system (m_c couples to J_r through a linear spring k_3 and with a clearance δ). **d** Conceptual diagram of the double-ultra mechanism using chaotic bands. LR1 (LR2) represents the first (second) LR bandgap induced by the linearized Duffing and vibro-impact systems, respectively. The black (dashed black) arrow represents the input wave u_{in} (its transmission) in linear resonant passbands and the red arrows represent the frequency components in the chaotic wave u_{out} . In **b**, **d**, the light blue (white) areas represent the band structure of the NAM (the corresponding LAM), where the blue lines are the upper limits of the chaotic bands

the band structure sketched in Fig. 1d, to demonstrate the double-ultra concept based on chaotic bands. The subwavelength meta-cell consists of a Duffing oscillator⁵¹ and a coupled vibro-impact system^{52, 53} (Fig. 1c). We expect passbands near LR1 and LR2 to become chaotic bands and reduce wave propagation. A nonlinear meta-cell (Fig. 2a) is achieved by the nonlinear force between permanent magnets and internal collisions. The primary structure is a linear uniform rectangular beam (or square plate) with density ρ and thickness h . The lattice constant and width of the beam are a and b , respectively. Each attached oscillator consists of three columniform magnets, a columniform strut and a bolt that is used to constrain the magnets. The entire attachment is fixed on the primary beam/plate at point O. At rest, the magnets are separated from one another by the same clearance Δ . The central magnet with mass m_r is the local resonator in the transverse direction. Other parameters are labeled in Fig. 2.

Nonlinear magnetostatic repulsion forces between the magnet m_r and the other two magnets⁵⁴ induce a transverse force $F(x)$ on m_r (see Methods):

$$F(x) \approx k_1x + k_2x^3, \quad (1)$$

where x is the deviation from the equilibrium position and $-\Delta < x < \Delta$. Therefore, the transverse motion of the attached oscillators can be treated as the Duffing system⁵¹ shown in Fig. 2a where m_0 is the equivalent concentrated mass added at point O. Its linear resonant frequency is f_r .

As shown in Fig. 2b, the flexural oscillation of the entire attachment is modeled as a linear torsional system $J_O - k_T - J_r$,

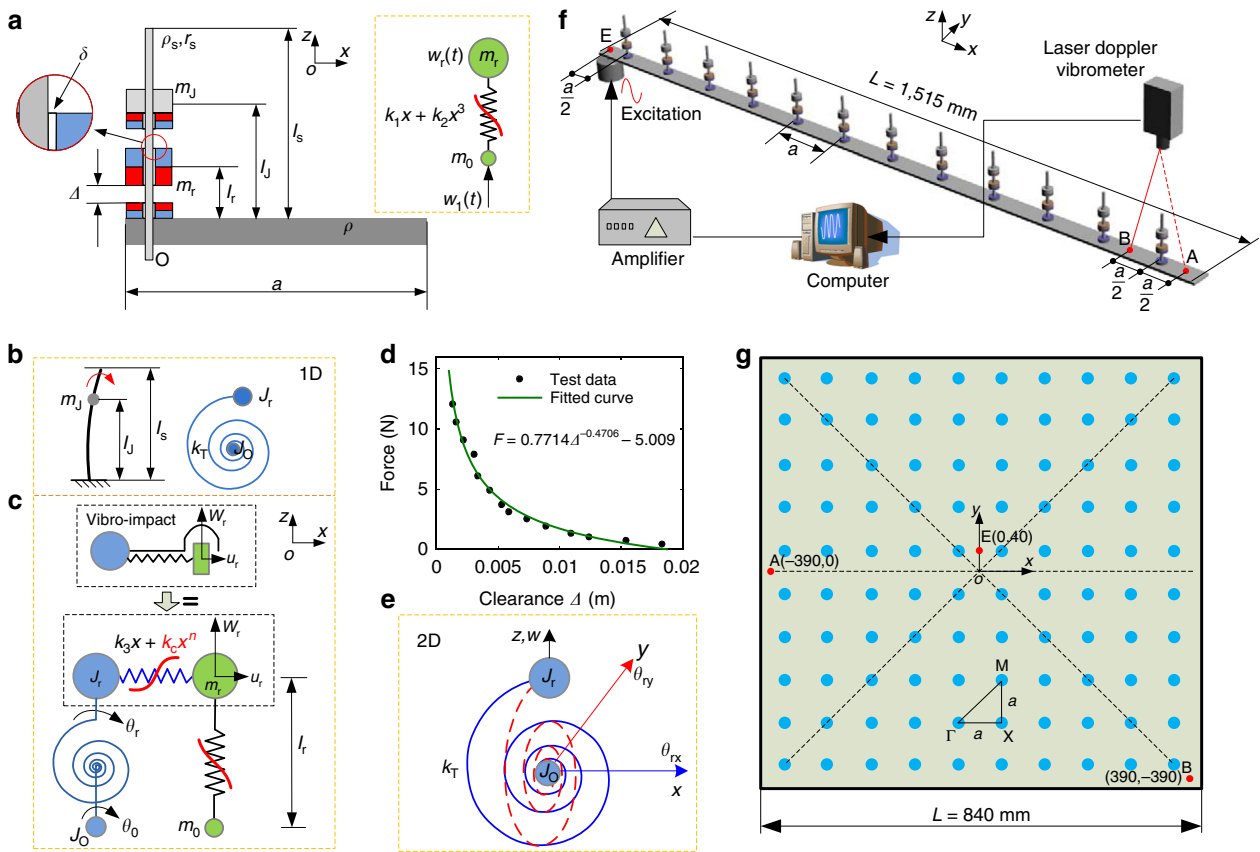


Fig. 2 Configurations of the NAM beam and plate. **a** Lateral view of the meta-cell with its parameters; the blue and red parts represent three magnets. The gray rectangle with length a is the principle beam/plate, and the columniform strut with length l_s is used to support the magnets. There is a clearance δ between the strut and the magnet m_r . The plot in the dashed box is the equivalent two-degrees-of-freedom (2DoF) Duffing model of the transverse motion of m_r . **b** Equivalent torsional motion of the whole attachment in the xz plane. **c** Whole equivalent coupling model for the attachment in NAM beam. **d** Repulsive force–clearance Δ relation of a pair of magnets. **e** Torsional system in 3D space for the 2D NAM plate. **f** The NAM beam consists of 12 periodic cells and the experimental apparatus. **g** The 2D NAM plate consisting of a square thin plate and 10×10 periodic attachments represented by blue points. In **f, g**, three red points, A, B and E, denote the measurement points, and E is also the excitation point. The positions of these points on the beam are labeled in **f**. For the plate, taking the center point of the square plate as the origin, the coordinates (x, y) of these points are labeled

where J_O is the inertia located at O, J_r is the free moment of inertia and k_T is the stiffness of the torsion spring connecting J_O and J_r (see Methods). As established, J_r also causes a negative index meanwhile the other LR bandgap in the metamaterials is near the natural frequency f_{T1} .

Moreover, the magnet features a central hole. A small clearance $\delta = 5 \times 10^{-4}$ m is left between the strut and the magnet m_r , and collisions occur in this clearance when the flexural amplitude becomes large. Therefore, the mass m_r generates two different nonlinear interactions during the motions along the transverse and longitudinal directions, respectively. Along the longitudinal direction, it is a vibro-impact oscillator⁵³ coupled to J_r through the nonlinear force $P(x)$ (see Methods):

$$P(x) = k_3 x + k_c x^n, \quad (2)$$

where $k_c = \alpha \delta^{-n}, \alpha \approx 1$. The linear part $k_3 x$ derives from the small longitudinal component of $F(x)$. As $\delta \ll \Delta$, a fair approximation for k_3 is $k_3 \approx k_1/10$. Parameter k_c becomes very large as n increases, e.g., $k_c \approx 1 \times 10^{10}$ N m⁻³ for $n = 3$, which indicates that it produces a strong nonlinearity under a smaller amplitude than in the Duffing oscillator. As a compromise, we use $n = 3$ to calculate periodic solutions. A comparative study for larger n is shown in Supplementary Fig. 5. Figure 2c shows the complete equivalent system for the NAM beam. However, for the NAM plate, the torsional motion is equivalent to two identical

coupled vibro-impact systems in 3D space (see Fig. 2e). The structural parameters are listed in Table 1 and other nonlinear factors are neglected in theoretical methods.

A NAM beam and a NAM plate consisting of periodic meta-atoms are shown in Fig. 2f, g and various parameters are listed in Table 2. The experimental methods and apparatuses are described in Methods.

Double-ultra 1D NAM beam. The transfer functions, dispersion curves, periodic solutions (i.e., frequency responses) and their bifurcations of the NAM beam are illustrated in Fig. 3. Transfer functions are defined as $H_{A(B)}(\omega) = 20 \log_{10}[X_{A(B)}(\omega)/X_E(\omega)]$, where $X(\omega)$ denotes the frequency spectrum and the subscripts A, B and E represent specific measurement points. We compare the dispersion solutions (Fig. 3b, c) and frequency responses (Fig. 3d) of the NAM beams considering only the Duffing oscillator (NAM-N1) and considering both the Duffing and vibro-impact oscillators (NAM-N2) (see Methods).

Four levels of broadband white noise were used to stimulate the NAM beam, as shown in Fig. 3a. From cases i to iv, the nonlinearity strength σ (see Methods) increases from 0 (linear) to 4.22 (strongly nonlinear). In both cases i and ii, σ is so small that the beam behaves similar to a LAM. The linearized ($k_2 = 0, k_c = 0$) dispersion curves for NAM-N1 and NAM-N2 are similar, except that another curve at 10.7 Hz, corresponding to the linearized

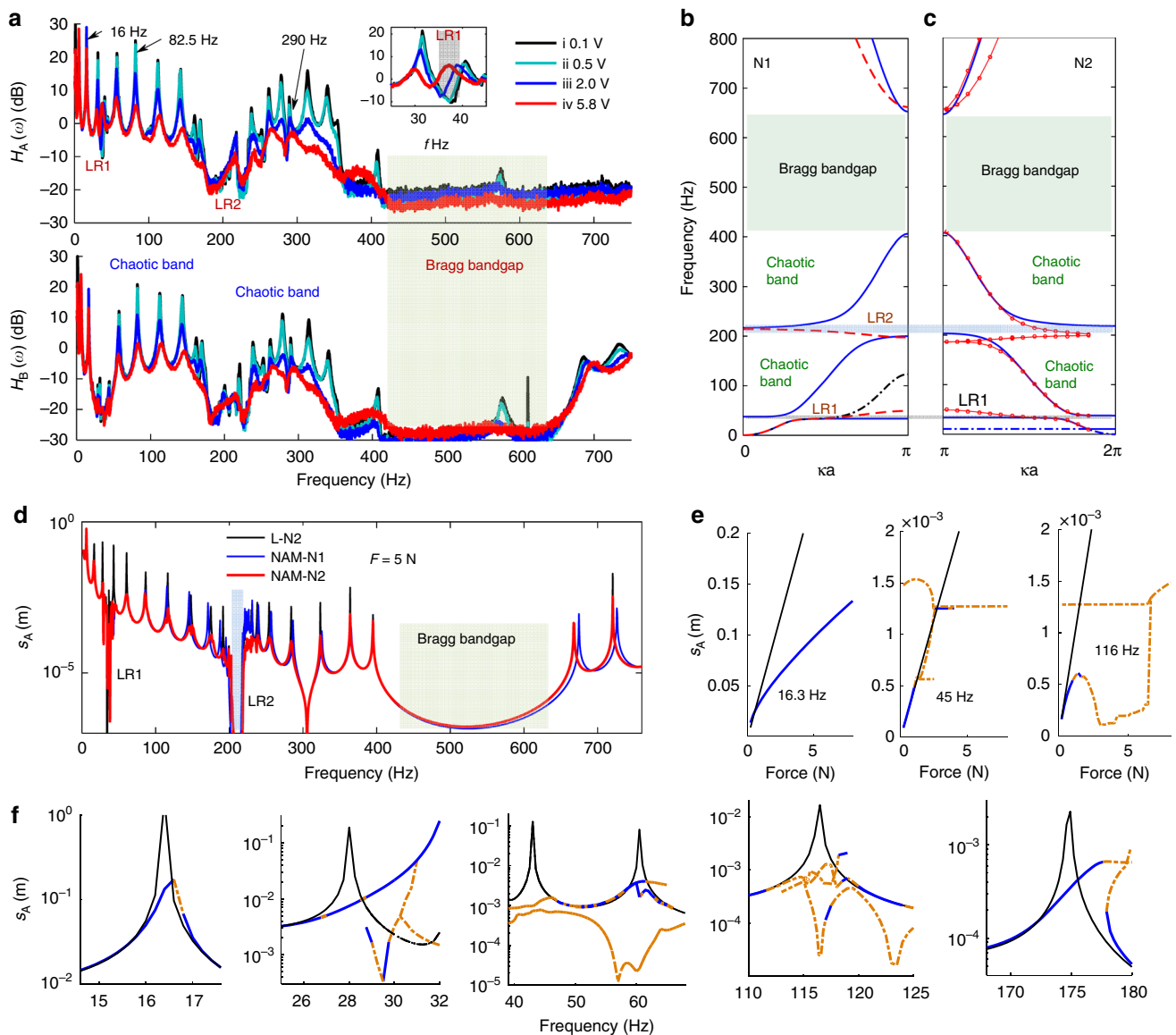


Fig. 3 Transfer functions, dispersion curves, responses and bifurcations of the NAM beam. **a** Transfer functions of points A and B under four levels of white-noise excitations. The average displacements in the interval (0, 20 Hz) represent the broadband excitation levels; (i: 0.1 V (the voltage of the amplifier), 1.06×10^{-3} mm (the average displacement), $\sigma = 7.5 \times 10^{-4} \approx 0$ (the nonlinearity strength)); (ii: 0.5 V, 6.453×10^{-3} , $\sigma = 0.028$); (iii: 2.0 V, 3.719×10^{-2} , $\sigma = 0.9262$); and (iv: 5.8 V, 7.936×10^{-2} , $\sigma = 4.22$). The small plot is the enlarged view near LR1. **b, c** Half dispersion curves of the **(b)** NAM-N1 and **(c)** N2. κ : the wave vector. In **b, c**, blue lines: LAM; red lines (black dashed line): the NAM solved with the harmonic balance method (HBM) (perturbation approach, PA) with displacement in case iv. In **b**, only the first curve of the PA results and three curves of the HBM results are shown, because others superpose with the linear results. Three shadings denote the linear bandgaps. **d** Theoretical displacements at point A s_A of the NAM N1, NAM N2 and the linearized LAM in case N2 (L-N2) based on the finite element method (FEM) and HBM (see Methods). In **d, f**, the driving force at point E is $F = 5$ N. **e, f** Bifurcation diagrams under **e** the changing force and **f** the changing frequency. Thin black lines: solutions of LAM; solid blue (dashed yellow): stable (unstable) periodic solutions of the NAM

vibro-impact oscillator, appears in N2 (Fig. 3b, c). However, this curve is nearly horizontal, thus no gap opens up. There are two LR bandgaps and a Bragg bandgap below 800 Hz: LR1 near f_r (33.5–37.8 Hz, $\gamma_{lr1} = 0.13$) induced by the linearized Duffing oscillator and LR2 near f_{T1} (200–230 Hz, $\gamma_{lr2} = 0.15$) induced by the torsional motion coupled with the vibro-impact oscillator. The Bragg bandgap in 420–660 Hz ($\gamma_{bg} = 0.57$) is relatively broad. Point B is the node of the flexural modes near f_f ; therefore, a small $H_B(\omega)$ is obtained in this range. Both $H_A(\omega)$ and $H_B(\omega)$ accurately reproduce the locations of the bandgaps, demonstrating that the theoretical methods are accurate. For the LAM beam, we obtain $\gamma_i < 1$ and $\sum \gamma_i = 0.85$; the passbands are linear resonant

bands in which resonances amplify the waves. The two basic properties make obtaining an ultra-low and broad bandgap to suppress waves in the LAM challenging.

The periodic nonlinear meta-cells create amplitude-dependent properties. In the strongly nonlinear case iv, the nonlinear dispersion solutions for N1 show that the nonlinearity shifts the peak of the first dispersion curve upward; thus, LR1 disappears. Figure 3a demonstrates that enhancing the nonlinearity increases the transmission in LR1 and makes it disappear in case iv. For N2, the curve at 10.7 Hz disappears and LR2 shifts downwards because the high nonlinear stiffness $3k_c x^2$ makes the spring become rigid, which is the limit dispersion solution⁴⁸ under a

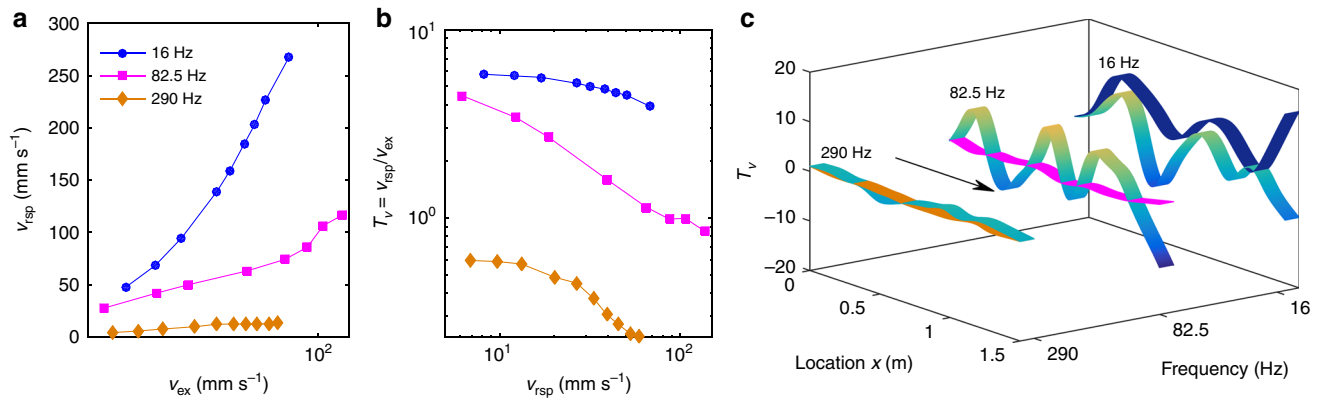


Fig. 4 Steady responses and wave modes of the NAM beam. **a** v_{rsp} and **b** T_v as a function of v_{ex} ; the horizontal axes are logarithmic scales. **c** Generalized wave modes of the whole beam under a small excitation (0.3 V, linear regime, shown by the rainbow colors) and a large excitation (5 V, strongly nonlinear regime, shown by the deep blue (16 Hz), magenta (82.5 Hz) and yellow (290 Hz) stripes)

large amplitude. The shifting of LR2 is not noticeable in experiments, because this limit solution overestimates the wave amplitudes, as further demonstrated in Fig. 3d. LR1 and LR2 are termed as nonlinear LR bandgaps. In both N1 and N2, additional curves in LR2 and near the fourth passband of harmonic balance method (HBM) solutions represent unstable waves that do not appear in practice⁴⁸, as indicated by $H_{A(B)}$.

Notably, the nonlinearity strongly influences wave propagation in the second and the third passbands, including a small region below LR1. From cases i to iv, relative to the resonant peaks, the wave transmission through the NAM beam decreases by ~20–40 dB in the ultra-low and ultra-broad band of 30–660 Hz (it is ~20 dB in the passbands and it is ~40 dB in the bandgaps). The generalized width reaches $\gamma = 21$, which constitutes a breakthrough compared with conventional LAMs (Supplementary Fig. 7). Therefore, the passbands of the strongly nonlinear AMs can significantly attenuate the elastic waves and enables subwavelength properties with $a = \lambda_l/9$ (see Methods). In the first passband, the influences of the nonlinearity on the three resonances are: significant for 31.56 Hz, moderate for 16 Hz ($H(\omega)$ decreases by 8 dB) and weak for 6 Hz ($H(\omega)$ unchanged), suggesting that the lower the resonance frequency below LR1, the weaker the effect of the nonlinearity^{47, 49}.

The frequency responses of the LAM and NAM beams confirm the previously detailed properties, as summarized in Fig. 3d (Supplementary Figs. 6, 7). The resonances and bandgaps derived from the theory are in good agreement with the measured $H(\omega)$. However, some discrepancies occur because the parameters and boundary conditions in the theoretical model do not perfectly reproduce the experimental conditions.

A moderate force $F = 5$ N causes the NAM to behave as a strongly nonlinear system (see Fig. 3d). The differences between N1 and N2 illustrate that: the periodic Duffing oscillators are responsible for the wave suppression near LR1 but its influence decreases with increasing distance to LR1 (both below and above LR1); and the vibro-impact oscillators are responsible for wave suppression in the two passbands on both sides of LR2 (Supplementary Note 3). As shown by NAM-N2, LR1 becomes a passband and the resonances in the second and the third passbands are substantially reduced because the linear resonances are replaced by the nonlinear resonances with finite amplitude⁴⁷. The experimental results agree well with the theoretical findings here and that from the discrete models^{47–49}, supporting the proposed mechanism for nonlinear wave propagation and the band structure of NAMs.

Furthermore, to theoretically demonstrate the chaotic mechanisms of the double-ultra properties and analyze the bifurcations of

periodic solutions, a dimension-reduction algorithm combined with other methods must be adopted (see Methods). As illustrated in Fig. 3e, f, multiple branches are found with the continuation algorithm⁴⁹ (Supplementary Note 4). Under a constant force, nonlinear resonances lower than LR1 lead to larger ranges for stable periodic solutions. However, for nonlinear resonances higher than LR1, only unstable branches or alternative stable and unstable solutions are found near the bending peaks. These unstable solutions and alternative properties have been addressed to induce chaos⁴⁹. Under 16.3 Hz (see Fig. 3e), only a monotonous stable branch is found; its amplitude is smaller than the linear solution and the first derivative decreases with increasing force. For the other two cases in Fig. 3e, the nonlinear solutions start along the linear branch and remain stable for a small force; however, then only unstable branches (or a small range of stable solutions), whose amplitudes remain nearly constant, are present, and consequently the transmission decreases. According to these bifurcation properties, it can be predicted that the NAM beam features a quasiperiodic or weakly chaotic response with less ability to reduce the wave transmission near 16.3 Hz. With regard to the waves in the second and the third passbands, they become strongly chaotic and exhibit larger transmission losses⁴⁹. These phenomena are experimentally evidenced in Fig. 4a–c.

To further understand the wave suppression in different bands and to demonstrate the chaotic mechanism observed, we studied the steady responses of the metamaterial at three representative frequencies, 16 Hz, 82.5 Hz and 290 Hz, in the first, the second and the third passbands, respectively. All are near (but not coincident with) the linear eigenfrequencies (see Fig. 3a). In Fig. 4, the transmission $T_v = v_{rsp}/v_{ex}$, where v_{rsp} and v_{ex} represent the velocity amplitudes at points A and E, respectively. In contrast to linear cases, here T_v rapidly decreases to a value less than 1, whereas v_{rsp} increases with the increasing v_{ex} . This behavior demonstrates that a stronger nonlinearity corresponds to a larger transmission loss⁴⁷ in the studied nonlinear range. Furthermore, T_v at 82.5 Hz and 290 Hz decrease more than at 16 Hz, in good agreement with the results in Fig. 3. In Fig. 4c, these wave reduction and suppression effects are further described by the generalized wave fields along the beam.

Double-ultra 2D NAM plate. The results of the scanning experiments (see Methods) on the 2D NAM plate are shown in Fig. 5a, b. As with the beam, from cases i to iv, the average driving displacement increases by 22 times and σ increases from $\sigma \approx 0$

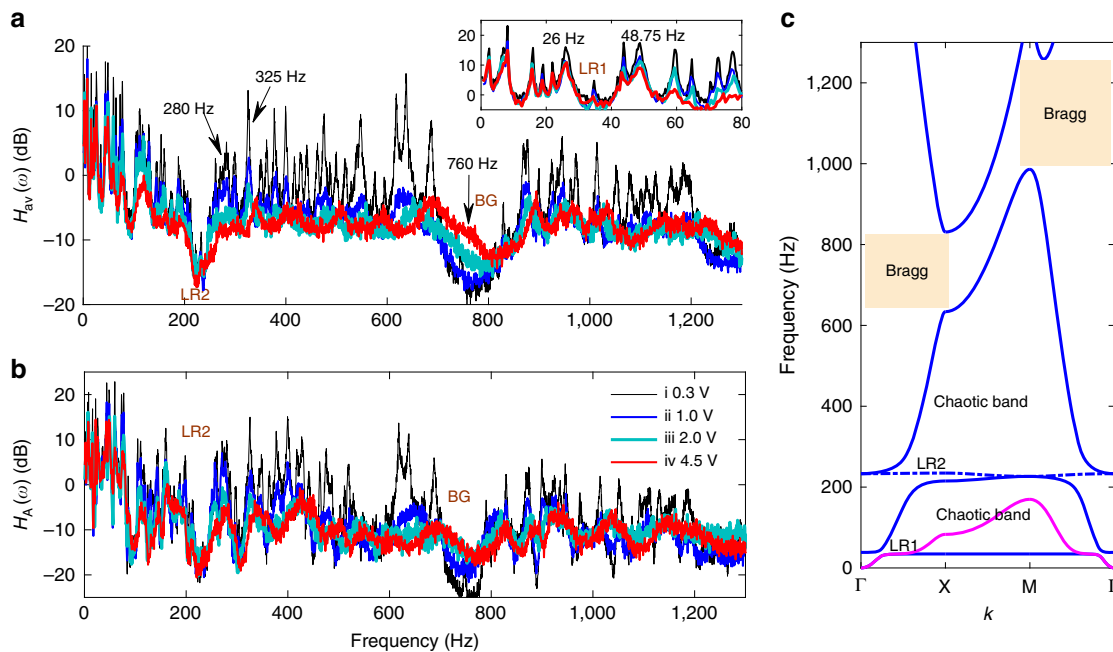


Fig. 5 Transfer functions and dispersion of the NAM plate. Excitations are broadband white noises. Four driving levels are (i: 0.3 V, 3.2578×10^{-3} mm, $\sigma = 0.0067 \approx 0$); (ii: 1.0 V, 1.5748×10^{-2} , $\sigma = 0.157$); (iii: 2.0 V, 3.2509×10^{-2} , $\sigma = 0.669$); (iv: 4.5 V, 7.1242×10^{-2} , $\sigma = 3.21$). **a** Average transfer function $H_{av}(\omega)$ of the 13×13 scanning points; the iconograph is the enlarged view near LR1. **b** Transfer functions of point A, $H_A(\omega)$. BG denotes Bragg bandgap. **c** Dispersion curves of the 2D metamaterial plate considering only the Duffing oscillator; blue curves: LAM; and magenta line: NAM solved with perturbation approach with displacement amplitude in case iii, other curves are superposed with blue curves (see Methods). k denotes the wave vector of the first Brillouin zone (see Fig. 2g)

(linear) to $\sigma = 3.21$ (strongly nonlinear). The average transfer function is $H_{av}(\omega) = \sum_{i=1}^N H_i(\omega)/N$, where $N = 169$.

As shown in Fig. 5c, two omnidirectional LR bandgaps open up near $f_{lr1} = 34.65$ Hz (34.5–38 Hz, $\gamma_{lr1} = 0.1$) and $f_{lr2} = 230$ Hz (216–245 Hz, $\gamma_{lr2} = 0.14$) because of the transverse motion of m_r and the coupled vibro-impact system, respectively. The dashed line in LR2 corresponds to the LR mode of the described torsional motion. Both LR1 and LR2 are nonlinear bandgaps. In addition, two directional Bragg bandgaps exist along ΓX and ΓM in the interval 635–835 Hz ($\gamma_{\Gamma X} = 0.32$) and near 1,150 Hz, respectively. However, $\gamma_i \ll 1$ and $\sum \gamma_i = 0.56$; thereby, they are narrow. The LR bandgaps are clearly visible in $H_{av}(\omega)$ and $H_A(\omega)$, as displayed in Fig. 5a, b. The directional bandgap along ΓX also helps suppressing the average response. Because of the dense flexural modes in this 2D LAM, the passbands feature dense resonances that enhance the incident waves.

For the 2D NAM plate, the perturbation result shows that the first dispersion curve gets significantly distorted because of the occurrence of the strong nonlinearity. In contrast to the linear case i, the strengthened nonlinearity suppresses the broadband resonances. In fact, a moderate nonlinearity in case ii enables suppression of the resonances between 30 and 1,200 Hz, especially in the range 200–1,200 Hz. Further enhancing the nonlinearity, as in case iv, leads to reductions both of $H_{av}(\omega)$ by 20–40 dB in the range 50–1,200 Hz and of the resonances by 10 dB in the range 30–50 Hz. We obtain a subwavelength property with $a = \lambda_r/10$ at 30 Hz here. Resonances in the first passband are minimally reduced. This behavior is the same as that observed in the NAM beam. Therefore, between 30 and 1,200 Hz this 2D NAM features the double-ultra property that the wave transmission is significantly reduced. The generalized width $\gamma = 39$ is nearly double the width of the NAM beam.

To further describe the double-ultra properties, we measured the steady responses at points A and B after a monochromatic excitation at point E (see Fig. 6). As expected, the 2D nonlinear

flexural mode depends on both the frequency and the position, and the transmission does not vary monotonically. At 26 Hz (Fig. 6a, e), although v_{rsp} increases with the increasing driving amplitude, T_v reaches the maximum value at $v_{ex} = 0.8$ mm s $^{-1}$ but then decreases by a factor of 2.7 at $v_{ex} = 9$. A similar behavior is observed at 48.75 Hz (Fig. 6b, f). In contrast, v_{rsp} at 280 Hz (Fig. 6c, g) and 325 Hz (Fig. 6d, h) first increase monotonically against v_{ex} and then remain nearly constant, while the transmission decreases substantially. Moreover, in the four cases except for a small region near $v_{ex} = 0.9$ mm s $^{-1}$ at 325 Hz, the amplitude and transmission at A and B vary synchronously.

As shown in Fig. 5a, b, $H(\omega)$ along ΓX for frequencies in the directional bandgap near 760 Hz increases with σ . Different experiments were conducted at 760 Hz to illustrate this effect. As shown in Fig. 7a, when increasing v_{ex} from zero, the waves are first suppressed so the responses vary along a low-energy orbit corresponding to the bounded state. The responses then jump up to a high-energy orbit at a critical point, that is, the excited state. With decreasing excitation, the responses jump down to the bounded state at a smaller critical point: a hysteresis loop is observed between the two states. The jump is relevant to saddle-node bifurcations^{49, 55}. In Fig. 7b, the contour plot of ΔT_v illustrates that elastic energy is transferred from the central area to the boundaries in the excited state, which breaks the bandgap effect. Therefore, the bandgaps in NAMs feature multi-state behavior switching from one state to the other by jumps⁴⁹. High-dimensional acoustic devices based on such behavior are conceivable.

Confirmation of chaotic waves in experiments. The double-ultra properties are relevant to the propagation states of the waves: periodic, quasiperiodic or chaotic. To understand the transition between periodic and chaotic states, and to further clarify the chaotic features and band structures, we analyzed the

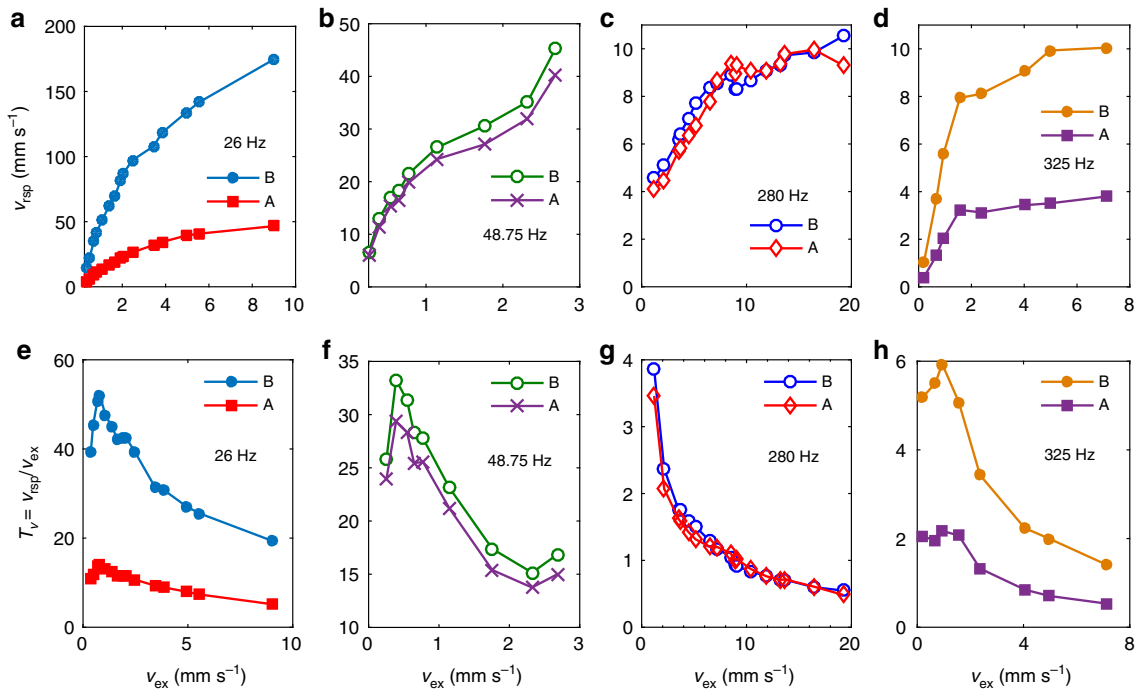


Fig. 6 Steady responses of the NAM plate. **a-d** Steady response amplitudes v_{rsp} and **e-h** the corresponding transmissions T_v at points A and B changing with v_{ex} under four frequencies 26, 48.75, 280 and 325 Hz in the first, the second and the third passbands, as labeled in Fig. 5a. In each legend, the frequency indicates that the diagram is relevant to this frequency and A (B) denotes v_{rsp} or T_v at point A (B) under that frequency

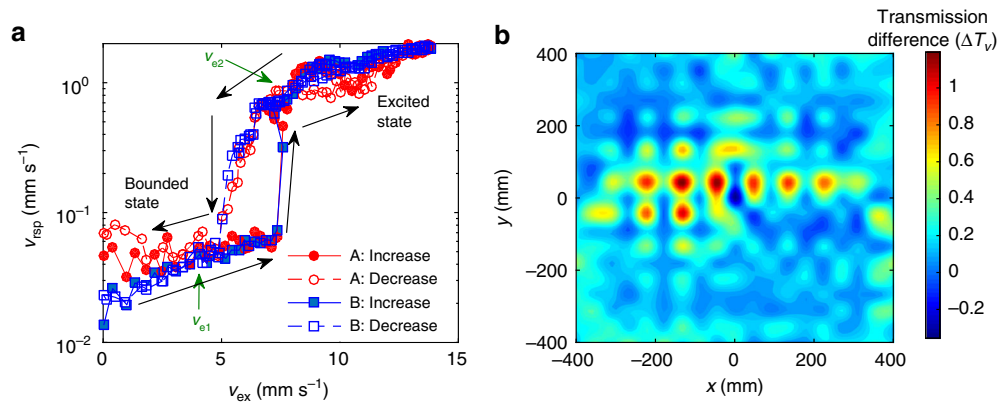


Fig. 7 Multi-states in the bandgap of NAM plate. Frequency is 760 Hz. **a** Response amplitudes v_{rsp} at points A and B varying against the linearly and continuously varied driving amplitude v_{ex} in time domain, i.e., the varying-amplitude experiment (see Methods). In the legend, Increase (decrease) refers to the process increasing (decreasing) v_{ex} . Black arrows show the varying routes. **b** Contour plot of the transmission difference ΔT_v between $v_{e1} = 3.13$ and $v_{e2} = 8.55$ labeled in **a**, $\Delta T_v = T_{v2} - T_{v1}$. Scanning experiments were carried out to obtain this plot

spectra and the largest Lyapunov exponents (LLEs, λ_m)^{50, 56–58} (see Methods) of the steady waves.

Theoretical investigations^{47–49} have revealed that the resonances are suppressed by the chaos induced by periodic-doubling bifurcations. The power spectra $P_A(\omega)$ at 290 Hz in the NAM beam (see Fig. 8a) clearly illustrate the period-doubling route to chaos. In the linear regime ($v_{rsp} = 3.137 \text{ mm s}^{-1}$), the energy is localized at the driving frequency f_d ; increasing v_{rsp} to 9.77 mm s^{-1} generates period-doubling frequencies that divides the elastic energy; further increasing the amplitude redistributes the wave energy in a broad, higher band, which is chaotic. This phenomenon has been termed energy dispersion⁴⁷.

First, we analyzed the LLEs of the NAM beam at the three frequencies in Fig. 4. As shown in Fig. 8b, LLE of the driving velocity fluctuates near 0 (see Methods) over a large amplitude

range. The maximum value < 0.05 is positive but small, ensuring that noises in the driving forces have a negligible influence, even if the forces are large. By considering the errors, $\lambda_{mc} = 0.05$ is chosen as the critical value of LLE where switching from the quasi-periodic to chaos occurs. In Fig. 8b, c, λ_m fluctuates in a non-monotonic way but still exhibits an increasing trend on the whole; when v_{ex} is very small, $\lambda_m < \lambda_{mc}$, indicating that the responses are periodic (or quasiperiodic). Further increasing v_{ex} causes λ_m to rapidly pass through zero and λ_{mc} to satisfy $\lambda_{mc} \leq \lambda_m < \infty$, which indicates that the waves become chaotic. In the chaotic regime $\lambda_m \gg 0$, at 82.5 and 290 Hz, which implies that chaotic behaviors are strong and that the trajectories in the chaotic attractors quickly become separated. By contrast, $\lambda_m < 0.1$ at 16 Hz denotes the weak chaos that is approximate to a quasiperiodic orbit; therefore, the material has a weaker ability

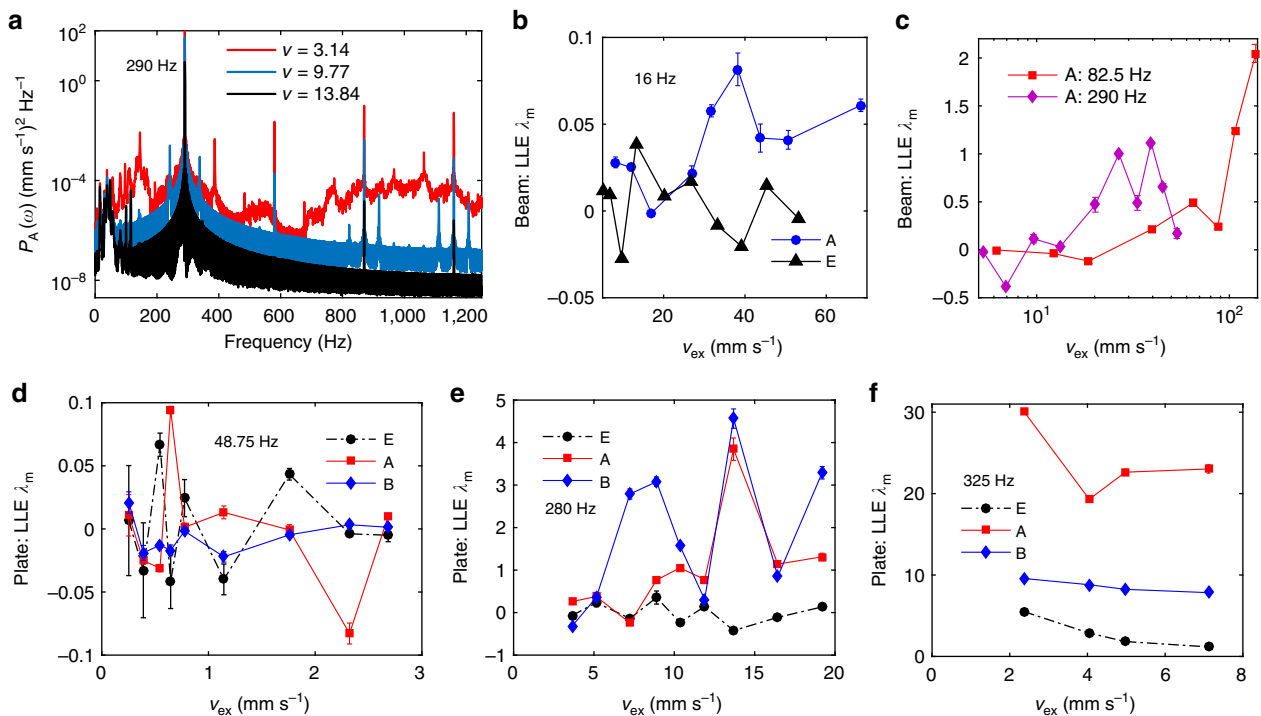


Fig. 8 Chaos and state transition in the NAMs. These signals under different frequencies are steady responses and excitations shown in Figs. 4, 6 for the beam and plate, respectively. **a** Power spectra $P_A(\omega)$ of point A under 290 Hz of the beam, the legend shows different response amplitudes. **b–f** Error graphs of the change of signal LLEs λ_m with v_{ex} , where the lengths of the bars indicate the computational errors; **b–c** for the beam and **d–f** for the plate. In the legends of **b–f**, A, B and E represent the signals at the corresponding measured points; every labeled frequency indicates λ_m under that frequency

to suppress the waves in frequency ranges below LR1⁴⁹. These results confirm the predictions made after the bifurcation analyses in Fig. 3e, f.

Next, we calculated λ_m of the NAM plate under the three frequencies in Fig. 6. The results obtained at 26 Hz are similar to those obtained at 48.75 Hz; therefore, only the latter are presented. At 48.75 Hz (see Fig. 8d), λ_m fluctuates near 0 and $\lambda_m < 0.1$ in the explored amplitude range at the three points E, A and B. Therefore, we deduce that low-frequency waves are periodic, quasiperiodic or weakly chaotic. At 280 Hz (Fig. 8e), λ_m at point E still fluctuates near 0; in contrast, λ_m at A and B increases to 4.5 so that strong chaos occurs, which suppresses the waves, and a periodic window appears at $v_{ex} = 11.89$. In the case of 325 Hz (Fig. 8f), the signal undergoes low-frequency noise therefore λ_m at point E has a large value. Fortunately, λ_m at points A and B are much larger, and $\lambda_m > 20$ at A, which corresponds to a strong chaos. Moreover, although the amplitudes measured at A and B are approximately equal (see Fig. 6), their LLEs differ substantially in some intervals, which indicates that although the amplitudes may vary synchronously at different points, one response may be strongly chaotic while the other is periodic.

The aforementioned quantitative statements experimentally establish that the passbands of the NAMs become chaotic, which agrees with the bifurcation analysis. Moreover, the regularities of the LLEs are mutually consistent with the theoretical findings outlined in the discrete model⁴⁹. Therefore, the experiments demonstrate the chaotic mechanism and the features of chaos in the NAMs.

Discussion

We designed a NAM beam and a plate with a strongly nonlinear meta-cell consisting of a Duffing oscillator and a linear torsional oscillator coupled to a vibro-impact oscillator. Our proof-of-

concept experimental results with the NAMs demonstrated that these metamaterials overcome the bandwidth limit ($\gamma < 1$) of conventional LAMs by at least two orders of magnitude: with subwavelength ($\sim \lambda_f/10$) cells, the generalized width reaches an exciting value $\gamma = 21$ in the 1D NAM and it increases to $\gamma = 39$ in the 2D NAM. In these broad bands (which consist of bandgaps and chaotic bands), the transmission of waves is reduced by as much as 20–40 dB. We demonstrated both theoretically and experimentally that the double-ultra effect is attributable to strong chaos, because the propagating elastic waves become chaotic under periodic incidents. The band structures and features of chaos are also consistent with the theoretical results. Moreover, bandgaps in the NAM exhibit a multi-state behavior; switching from one state to the other arises by jumps.

In conclusion, this study demonstrates the chaotic band in NAMs, which can significantly reduce the wave transmission in an ultra-low and ultra-broad band. Our work unveils the physical effects of NAMs and enables further progress in understanding NAMs. We envision that the chaotic band induced double-ultra wave suppression will open new opportunities for vibration and noise control, acoustic energy transfer and dissipation and elastic wave manipulation. The multi-state behavior presents an advantage in controlling the state of acoustic devices.

Methods

Metamaterial samples. The parameters of the NAM samples shown in Fig. 2 are listed in Table 1. The permanent magnet is made of the neodymium–iron–boron alloy. Its outer diameter, inner diameter and the thickness are 15, 5 and 4 mm, respectively. The oscillator m_t consists of two magnets. A magnet is fixed on both the beam and the bolt, respectively, that is the installation scheme of the magnets is one–two–one. In Fig. 2a, ρ_s (r_s) denotes the density (the radius) of the strut; m_t denotes the total mass of the upper magnet and its bolt.

The flexural wavelength of the primary structure is

$$\lambda_f = 2\pi(EI/\rho_b h)^{1/4} \omega^{-1/2}, \quad (3)$$

Table 1 Parameters of the NAMs

Para.	a (mm)	b (mm)	h (mm)	m_O (g)	m_r (g)	m_j (g)
1D	120	20	3.8	15	10	9
2D	80	-	2	8	10	9
Para.	Δ (mm)	l_r (mm)	l_j (mm)	l_s (mm)	r_s (mm)	λ_f (m)
1D	12.5	20.5	45	70	1.9	1.074
2D	12	20	40	70	1.9	0.805

Here λ_f denotes the flexural wavelength at 30 Hz

Table 2 Equivalent parameters of the attached structure

Para.	k_1 (N m ⁻¹)	k_2 (N m ⁻³)	J_O (kg m ²)	J_r (kg m ²)	k_T (N m rad ⁻¹)
1D	448.67	3.276e6	5.750e-7	2.225e-5	44.874
2D	473.92	2.93e6	5.820e-7	1.838e-5	49.045

where E is elastic modulus and $I = bh^3/12$. The flexural wavelength in the pure plate is

$$\lambda_f = 2\pi(D_0/\rho h)^{1/4} \omega^{-1/2}, \quad (4)$$

where ω denotes the angle frequencies; $D_0 = Eh^2/12(1-\mu^2)$; ρ and μ are the density and the Poisson's ratio of the material, respectively. The beam, the plate and the struts are all made of aluminum. It's $E = 70$ GPa, $\mu = 0.3$ and $\rho = 2,780$ kg m⁻³.

Equivalent motions. The magnetostatic repulsion force between the permanent magnets can be expressed as $F(\Delta) = C\Delta^{-p} + C_0$, $p > 0$, where C and C_0 are constants. C_0 is introduced to better fit the measured data and in theory $C_0 = 0$. Therefore, the transverse force (along z axis) on m_r reads⁵⁴ $F(x) = C[(\Delta-x)^{-p} - (\Delta+x)^{-p}] \approx k_1x + k_2x^3$, i.e., Eq. (1). We measured the nonlinear repulsive force-clearance relation $F(\Delta)$ between two identical magnets, as illustrated in Fig. 2d. The stiffness coefficients k_1 and k_2 derived from the measurements are listed in Table 2. Because of the cubic nonlinear term k_2x^3 in Eq. (1), the transverse attached oscillators can be treated as the Duffing system⁵¹ represented in Fig. 2a. Its transverse motion equations read

$$m_O \ddot{w}_1 = F_1(t) + k_1(w_r - w_1) + k_2(w_r - w_1)^3, \quad (5)$$

$$m_r \ddot{w}_r = -k_1(w_r - w_1) - k_2(w_r - w_1)^3, \quad (6)$$

where w_1 and w_r are transverse displacements of m_O and m_r , respectively; $F_1(t)$ is the node force applied on m_O , which is generated by the shearing stress in the beam or plate; the double overdot denotes a second-order time derivative. The linearized natural frequency of this Duffing oscillator is $f_f \approx 35$ Hz.

Moreover, the bending moment causes the entire attachment undergoing flexural oscillations (see Fig. 2b). This part is modeled as a small beam attached with a concentrated masse m_j at the location l_j , which induces a considerable moment of inertia. Therefore an entire attachment in low frequency is equivalent to the linear torsional system $J_O - k_T - J_r$.

In fact, the collision occurs in the small clearance δ when the torsional amplitude is not small, which provides the other strongly nonlinear source in our NAMs. The elastic impact interaction force follows the power law⁵³ $\alpha(x/\delta)^n = k_c x^n$, $k_c = \alpha \delta^{-n}$, where $n > 1$ is an odd number and α depends on the estimated peak force (or acceleration) in the collision. The value of δ^{-n} is so large that the influence of α becomes weak, here $\alpha \approx 1$. The function becomes rectangular if $n \rightarrow \infty$. Therefore, the motion of m_r along the longitudinal direction is a vibro-impact oscillator that couples with J_r through the nonlinear force $P(x)$ in Eq. (2). For the NAM beam, the torsion motion of the entire attachment occurs in the xz plane only and the complete equivalent system of a cell is shown in Fig. 2c. The motion equations of this coupling nonlinear system are

$$J_O \ddot{\theta}_O = k_T(\theta_r - \theta_O) + M_O(t), \quad (7)$$

$$J_r \ddot{\theta}_r + m_r l_r \ddot{u}_r = -k_T(\theta_r - \theta_O), \quad (8)$$

$$m_r \ddot{u}_r = -k_3(u_r - l_r \theta_r) - k_c(u_r - l_r \theta_r)^n, \quad (9)$$

where θ_O and θ_r are torsional angles of J_O and J_r , respectively; $M_O(t)$ is the bending moment generated by the primary beam and u_r is the longitudinal displacement of

m_r . Other nonlinear factors are analyzed and can be neglected (see Supplementary Figs. 4, 6).

For the uncoupled 2DoF torsional system, by equations $\ddot{\theta}_O = -\omega^2 \theta_O$, $\ddot{\theta}_r = -\omega^2 \theta_r$, we can solve θ in terms of θ_O , so that, in terms of the angle θ_O , one yields

$$M_O = \bar{J}(\omega) \ddot{\theta}_O, \quad (10)$$

$$\bar{J}(\omega) = J_O + k_T/(\omega_{OT}^2 - \omega^2), \quad (11)$$

where $\omega_{OT}^2 = k_T/J_r$ and $\bar{J}(\omega)$ symbolizes the equivalent dynamic inertia of the whole attachment at frequency ω . This expression is similar to the LR oscillator in an AM³. $\bar{J}(\omega)$ indicates that the moment of inertia can also generate a negative index and introduces another LR bandgap in the metamaterial near the natural frequency $f_{T1} = \omega_{OT}/2\pi$. The three equivalent parameters, J_O , J_r and k_T , can be determined based on the FEM⁵⁹, as detailed in Supplementary Note 1. Their values are listed in Table 2, and $f_{T1} = 226$ Hz (Supplementary Fig. 1).

In the NAM plate, the bending moment in the plate drives the attachment to generate flexure motion in the 3D space (see Fig. 2e) but not in a 2D plane as the AM beam does. Therefore, the equivalent system has six DoFs and the motion equation of this part reads

$$J_O \ddot{\theta}_{Oi} = k_T(\theta_{ri} - \theta_{Oi}) + M_{Oi}(t), \quad (12)$$

$$J_r \ddot{\theta}_{ri} + m_r l_r \ddot{u}_{ri} = -k_T(\theta_{ri} - \theta_{Oi}), \quad (13)$$

$$m_r \ddot{u}_{ri} = -k_3(u_{ri} - l_r \theta_{ri}) - k_c(u_{ri} - l_r \theta_{ri})^n, \quad (14)$$

where θ and M denote the torsional angle and bending moment, respectively; $i = x, y$; subscripts x and y symbolize the coordinates x and y ; the subscripts r (O) represents the variables of the resonator (the fix point O on the plate). As the two systems are identical, by considering the oscillation in the xz plane only, we can obtain the equivalent parameters, which is same with the 1D beam. The results are listed in Table 2, and $f_{T1} = 260$ Hz, $f_{T2} = 1,484$ Hz.

The strength of nonlinearity is defined by

$$\sigma = nk_c A^{n-1}/k_3, \quad (15)$$

where A stands for the response amplitude used to estimate the nonlinear strength^{47, 49}. σ is a relative indicator. A larger σ is the stronger is the nonlinearity.

Experiment apparatuses and measurements. The experimental configuration and testing scheme for the NAM beam and plate are shown in Fig. 2. The metamaterial beam and plate were fixed to an electromagnetic exciter at point E. The output driving velocities and displacements were adjusted by modulating the voltage of the amplifier.

For the NAM beam, the other end was free; two test points on the primary beam, A and B, were set on the symmetrical sides of the 12th attachment (see Fig. 2f). Two types of experiments were implemented with the NAM beam: broadband frequency responses and responses under monochromatic excitations. For the broadband responses, the random broadband white noise acted as the driving force and the response velocities at points A, B and E, were directly measured. In the other experiment, monochromatic sinusoidal waves were employed to drive the beam, and the responses in the time domain at points A and E were measured. In both experiments, the response velocities at the three points were measured synchronously using three laser Doppler vibrometers. In addition, for the measurement of the wave shapes of the whole beam, a vibrometer was used to scan points along the primary beam.

For the NAM plate, the excitation point E was near but not coincident with the center point of the plate. Other boundaries of the plate were free. This driving method can excite the non-symmetrical modes of flexural waves in the plate. The positions of measurement for points A, B and E are shown in Fig. 2g. The two types of experiments were also implemented on the 2D NAM plate. However, in the broadband frequency responses experiment, 13×13 scanning points were set on the primary plate, and a vibrometer was used to measure their velocities one by one. In addition, we used a varying-amplitude monochromatic experiment to measure multiple states in the bandgap. Here the driving amplitude was $A(t) \sin(2\pi f_d t)$, where f_d is constant but the amplitude $A(t)$ changes linearly with time. Moreover, to measure the wave fields in the bounded state and excited state under 760 Hz, 19×19 scanning points were set on the primary plate. In the scanning experiments, the measured points were distributed uniformly in a square region from the coordinate $(-400, 400)$ to $(400, -400)$.

Signal processing. Nonlinear time series analysis methods were employed to analyze signals under monochromatic excitations. Under periodic incidents, the propagated waves in the NAM beam follow periodic, quasiperiodic or chaotic trajectories⁵¹. The chaotic trajectories in its attractor diverge, on average, at an exponential rate over the time evolution characterized by the largest Lyapunov exponent (LLE) λ_m ⁵⁶. Therefore, the LLE can quantitatively identify whether the

signal is chaotic. In theory, if $\lambda_m < 0$, the motion is periodic having a stable fixed point; if $\lambda_m = 0$, it is a quasiperiodic response having a stable limit cycle; and if $0 < \lambda_m < \infty$, it is chaotic. However, errors and noises from the algorithm and experiment make using a single value $\lambda_m = 0$ to identify the quasiperiodic state in experiments almost impossible.

We employed an algorithm for the LLE derived by Kantz et al.^{56–58} because of its robustness to the noise; this algorithm is based on the phase space reconstruction technique. The proper embedding dimension d_E and time delay τ should be determined to reconstruct the phase space⁵⁶; the autocorrelation function was calculated to determine the optimal lag τ , and the false nearest neighbors method was used to determine the optimal d_E .

Dispersion theories. We established the finite element models of the meta-cells of both the NAM beam and plate. For NAM-N1, perturbation approach (PA) was used to calculate the approximate dispersion solutions. For NAM-N2, only the HBM could be used and the analytical solutions of the dispersion equations were solved. However, for the NAM plate-N2, the high dimensions of equations made finding analytical solutions difficult. Therefore, only the dispersion solution solved by PA of the NAM plate N1 is presented (see Supplementary Note 2 for more details).

Periodic solutions and bifurcations. A periodic solution is also a steady frequency response. To calculate the frequency responses, we used a standard finite element procedure⁵⁹ to obtain the motion equations for the whole NAM beam. Then, we used HBM to solve the approximate solutions. The numerical Newton method helps finding the solutions (Supplementary Note 3).

In the case NAM beam-N2, the finite element model has 90 dimensions. However, to analyze the stabilities and bifurcations of the periodic solutions, we need to reduce the dimensions of the whole model. We adopted the post-processed Galerkin algorithm in the frequency domain to reduce the dimensions of the NAM beam-N2 (Supplementary Note 4). A picking dimension-reduction procedure reduced the dimensions from 90 to 23. With the reduced system, we analyzed the periodic solutions and their bifurcations using the harmonic average method (Supplementary Figs. 8, 9).

Data availability. The experimental data that support the findings of this study are available in Dryad Digital Repository (<http://datadryad.org/>) with the identifier DOI:10.5061/dryad.6m8n⁶⁰.

Received: 21 March 2017 Accepted: 19 July 2017

Published online: 03 November 2017

References

- Liu, Z. et al. Locally resonant sonic materials. *Science* **289**, 1734–1736 (2000).
- Cummer, S. A., Christensen, J. & Alù, A. Controlling sound with acoustic metamaterials. *Nat. Rev. Mater.* **1**, 16001 (2016).
- Ma, G. & Sheng, P. Acoustic metamaterials: from local resonances to broad horizons. *Sci. Adv.* **2**, e1501595 (2016).
- Chen, Y., Liu, H., Reilly, M., Bae, H. & Yu, M. Enhanced acoustic sensing through wave compression and pressure amplification in anisotropic metamaterials. *Nat. Commun.* **5**, 5247 (2014).
- Wang, G., Wen, X., Wen, J., Shao, L. & Liu, Y. Two-dimensional locally resonant phononic crystals with binary structures. *Phys. Rev. Lett.* **93**, 154302 (2004).
- Ho, K. M., Cheng, C. K., Yang, Z., Zhang, X. & Sheng, P. Broadband locally resonant sonic shields. *Appl. Phys. Lett.* **83**, 5566–5568 (2003).
- Xiao, Y., Wen, J. & Wen, X. Longitudinal wave band gaps in metamaterial-based elastic rods containing multi-degree-of freedom resonators. *New J. Phys.* **14**, 033042 (2012).
- Zhang, H., Xiao, Y., Wen, J., Yu, D. & Wen, X. Ultra-thin smart acoustic metasurface for low-frequency sound insulation. *Appl. Phys. Lett.* **108**, 141902 (2016).
- Mei, J. et al. Dark acoustic metamaterials as super absorbers for low-frequency sound. *Nat. Commun.* **3**, 756 (2012).
- Pendry, J. B. & Li, J. An acoustic metafluid: realizing a broadband acoustic cloak. *New J. Phys.* **10**, 115032 (2008).
- Stenger, N., Wilhelm, M. & Wegener, M. Experiments on elastic cloaking in thin plates. *Phys. Rev. Lett.* **108**, 014301 (2012).
- Bückmann, T., Thiel, M., Kadic, M., Schittny, R. & Wegener, M. An elasto-mechanical unfeelability cloak made of pentamode metamaterials. *Nat. Commun.* **5**, 4130 (2014).
- Ni, X. et al. Topologically protected one-way edge mode in networks of acoustic resonators with circulating air flow. *New J. Phys.* **17**, 053016 (2015).
- Rupin, M., Lemoult, F., Lerosey, G. & Roux, P. Experimental demonstration of ordered and disordered multiresonant metamaterials for lamb waves. *Phys. Rev. Lett.* **112**, 234301 (2014).
- Moiseyenko, R. P., Pennec, Y., Marchal, R., Bonello, B. & Djafari-Rouhani, B. Broadband attenuation of Lamb waves through a periodic array of thin rectangular junctions. *Phys. Rev. B* **90**, 134307 (2014).
- Cai, L., Han, X. & Wen, X. Band-structure results for elastic waves interpreted with multiple-scattering theory. *Phys. Rev. B* **74**, 153101 (2006).
- Ma, G., Min, Y., Xiao, S., Yang, Z. & Sheng, P. Acoustic metasurface with hybrid resonances. *Nat. Mater.* **13**, 873–878 (2014).
- Zhao, J., Bonello, B. & Boyko, O. Focusing of the lowest-order anti-symmetric Lamb mode behind a gradient-index acoustic metalens with local resonators. *Phys. Rev. B* **93**, 174306 (2016).
- Kushwaha, M. S., Halevi, P., Dobrzynski, L. & Djafari-Rouhani, B. Acoustic band structure of periodic elastic composites. *Phys. Rev. Lett.* **71**, 2022–2025 (1993).
- Hussein, M. I., Leamy, M. J. & Ruzzene, M. Dynamics of phononic materials and structures: historical origins, recent progress and future outlook. *App. Mech. Rev.* **66**, 040802 (2014).
- Xiao, Y., Wen, J., Wang, G. & Wen, X. Theoretical and experimental study of locally resonant and Bragg band gaps in flexural beams carrying periodic arrays of beam-like resonators. *J. Vib. Acoustics* **135**, 041006 (2013).
- Xiao, Y., Wen, J. & Wen, X. Flexural wave band gaps in locally resonant thin plates with periodically attached spring-mass resonators. *J. Phys. D: Appl. Phys.* **45**, 195401 (2012).
- Lapine, M., Gorkunov, M. & Ringhofer, K. Nonlinearity of a metamaterial arising from diode insertions into resonant conductive elements. *Phys. Rev. E* **67**, 065601 (2003).
- Zharov, A. A., Shadrivov, I. V. & Kivshar, Y. S. Nonlinear properties of left-handed metamaterials. *Phys. Rev. Lett.* **91**, 037401 (2003).
- Zheludev, N. I. The road ahead for metamaterials. *Science* **328**, 582–583 (2010).
- Lapine, M., Shadrivov, I. V. & Kivshar, Y. S. Colloquium: nonlinear metamaterial. *Rev. Mod. Phys.* **86**, 1093–1123 (2014).
- Agranovich, V. M., Shen, Y. R., Baughman, R. H. & Zakhidov, A. A. Linear and nonlinear wave propagation in negative refraction metamaterials. *Phys. Rev. B* **69**, 165112 (2004).
- Zheludev, N. I. & Kivshar, Y. S. From metamaterials to metadevices. *Nat. Mater.* **11**, 917–924 (2012).
- Rose, A., Huang, D. & Smith, D. R. Controlling the second harmonic in a phase-matched negative-index metamaterial. *Phys. Rev. Lett.* **107**, 063902 (2011).
- Shadrivov, I. V., Fedotov, V. A., Powell, D. A., Kivshar, Y. S. & Zheludev, N. I. Electromagnetic wave analogue of an electronic diode. *New J. Phys.* **13**, 033025 (2011).
- Wang, Z. et al. Harmonic image reconstruction assisted by a nonlinear metamaterial surface. *Phys. Rev. Lett.* **106**, 047402 (2011).
- Fermi, E., Pasta, J. & Ulam, S. *Studies of Nonlinear Problems. Collected Papers II* 977–988 (University of Chicago Press, 1955).
- Gallavotti, G. *The Fermi-Pasta-Ulam Problem: A Status Report*, 1st edn, Vol. 728 (Springer, Berlin, 2008).
- Li, N. et al. Colloquium: phononics: manipulating heat flow with electronic analogs and beyond. *Rev. Mod. Phys.* **84**, 1045 (2012).
- Nesterenko, V. F. *Dynamics of Heterogeneous Materials*. (Springer, 2001).
- Nesterenko, V. F., Daraio, C., Herbold, E. B. & Jin, S. Anomalous wave reflection at the interface of two strongly nonlinear granular media. *Phys. Rev. Lett.* **95**, 158702 (2005).
- Daraio, C., Nesterenko, V. F., Herbold, E. & Jin, S. Tunability of solitary wave properties in one-dimensional strongly nonlinear phononic crystals. *Phys. Rev. E* **73**, 026610 (2006).
- Narisetti, R. K., Ruzzene, M. & Leamy, M. J. A perturbation approach for analyzing dispersion and group velocities in two-dimensional nonlinear periodic lattices. *J. Vib. Acoustics* **133**, 061020 (2011).
- Boechler, N. et al. Discrete breathers in one-dimensional diatomic granular crystals. *Phys. Rev. Lett.* **104**, 244302 (2010).
- Kim, E. et al. Highly nonlinear wave propagation in elastic woodpile periodic structures. *Phys. Rev. Lett.* **114**, 118002 (2015).
- Wang, S. Y. & Nesterenko, V. F. Attenuation of short strongly nonlinear stress pulses in dissipative granular chains. *Phys. Rev. E* **91**, 062211 (2015).
- Lydon, J., Theocharis, G. & Daraio, C. Nonlinear resonances and energy transfer in finite granular chains. *Phys. Rev. E* **91**, 023208 (2015).
- Liang, B., Yuan, B. & Cheng, J. C. Acoustic diode: rectification of acoustic energy flux in one-dimensional systems. *Phys. Rev. Lett.* **103**, 104301 (2009).
- Liang, B., Guo, X. S., Tu, J., Zhang, D. & Cheng, J. C. An acoustic rectifier. *Nat. Mater.* **9**, 989–992 (2010).
- Boechler, N., Theocharis, G. & Daraio, C. Bifurcation-based acoustic switching and rectification. *Nat. Mater.* **10**, 665–668 (2011).
- Donahue, C. M., Anzel, P. W., Bonanomi, L., Keller, T. A. & Daraio, C. Experimental realization of a nonlinear acoustic lens with a tunable focus. *Appl. Phys. Lett.* **104**, 014103 (2014).
- Fang, X., Wen, J., Yin, J., Yu, D. & Xiao, Y. Broadband and tunable one-dimensional strongly nonlinear acoustic metamaterials: theoretical study. *Phys. Rev. E* **94**, 052206 (2016).

48. Fang, X., Wen, J., Yin, J. & Yu, D. Wave propagation in nonlinear metamaterial multi-atomic chains based on homotopy method. *AIP Adv.* **6**, 121706 (2016).
49. Fang, X., Wen, J., Bonello, B., Yin, J. & Yu, D. Bifurcations and chaos in nonlinear acoustic metamaterials. *New. J. Phys.* **19**, 053007 (2017).
50. Strogatz, S. H. *Nonlinear Dynamics and Chaos: With Applications to Physics, Biology, Chemistry, and Engineering.* (Westview, Colorado, 2014).
51. Nayfeh, A. H. & Mook, D. T. *Nonlinear Oscillations* (Wiley, New Jersey, 1979).
52. Babitsky, V. I. *Theory of Vibro-Impact Systems and Applications* (Springer, Berlin, 1998).
53. Mikhlin, Y. V., Vakakis, A. F. & Salenger, G. Direct and inverse problems encountered in vibro-impact oscillations of a discrete system. *J. Sound Vib.* **216**, 227–250 (1998).
54. Fang, X., Wen, J., Yin, J. & Yu, D. Highly efficient continuous bistable nonlinear energy sink composed of a cantilever beam with partial constrained layer damping. *Nonlinear Dyn.* **87**, 2677–2695 (2017).
55. Bernard, B. P., Mazzoleni, M. J., Garraud, N., Arnold, D. P. & Mann, B. P. Experimental investigation of bifurcation induced bandgap reconfiguration. *J. Appl. Phys.* **116**, 084904 (2014).
56. Kantz H. & Schreiber, T. *Nonlinear Time Series Analysis*, 2nd edn, (Cambridge University Press, Cambridge, 2004)
57. Rosenstein, M. T., Collins, J. J. & De Luca, C. J. A practical method for calculating largest Lyapunov exponents from small data sets. *Phys. D* **65**, 117–134 (1993).
58. Kantz, H. A robust method to estimate the maximal Lyapunov exponent of a time series. *Phys. Lett. A.* **185**, 77–87 (1994).
59. Petyt, M. *Introduction to Finite Element Vibration Analysis*, 2nd edn, (Cambridge University Press, Cambridge, 2010).
60. Fang, X., Wen, J., Bonello, B., Yin, J. & Yu D. Wave propagation in one-dimensional nonlinear acoustic metamaterials. Pre-print at <https://arxiv.org/abs/1703.06761> (2017)

Acknowledgements

This research was funded by the National Natural Science Foundation of China (Projects Number 51405502, number 51275519 and number 11372346).

Author contributions

J.W. supervised the experiments; X.F. proposed the idea and designed the experimental proposal; X.F., J.W., J.Y. and D.Y. prepared the experimental set-up; X.F. performed the experiments; X.F. and B.B. carried out the theoretical calculations; X.F., J.W. and B.B. wrote the paper; all authors analyzed the data, discussed the results and commented on the manuscript.

Additional information

Supplementary Information accompanies this paper at doi:10.1038/s41467-017-00671-9.

Competing interests: The authors declare no competing financial interests.

Reprints and permission information is available online at <http://npg.nature.com/reprintsandpermissions/>

Publisher's note: Springer Nature remains neutral with regard to jurisdictional claims in published maps and institutional affiliations.



Open Access This article is licensed under a Creative Commons Attribution 4.0 International License, which permits use, sharing, adaptation, distribution and reproduction in any medium or format, as long as you give appropriate credit to the original author(s) and the source, provide a link to the Creative Commons license, and indicate if changes were made. The images or other third party material in this article are included in the article's Creative Commons license, unless indicated otherwise in a credit line to the material. If material is not included in the article's Creative Commons license and your intended use is not permitted by statutory regulation or exceeds the permitted use, you will need to obtain permission directly from the copyright holder. To view a copy of this license, visit <http://creativecommons.org/licenses/by/4.0/>.

© The Author(s) 2017